RSC Advances

PAPER

Cite this: *RSC Adv.*, 2026, **16**, 29703

Theoretical investigation of the magnetic semiconductor nature in PbI_2 monolayer induced by Fe doping

Huynh Thi Phuong Thuy,[a] Do T. Hue,[b] Thi Hue Trinh,[c] Vo Van On,[d] J. Guerrero-Sanchez[e] and D. M. Hoat*[fg]

Transition metal doping in two-dimensional (2D) semiconductor materials is an efficient way to develop new spintronic materials. In this work, the effects of Fe doping on the PbI_2 monolayer electronic and magnetic properties are investigated using first-principles calculations. The pristine PbI_2 monolayer is an indirect-gap semiconductor with a band gap of 2.50 eV. Fe doping induces effective magnetism engineering in this 2D material with a total magnetic moment of 4.00 μ_B and in-plane magnetic anisotropy (IMA). Herein, the magnetism is produced mainly by Fe impurities. Parallel spin coupling with perpendicular magnetic anisotropy (PMA) is found in the monolayer doped with two Fe atoms ($2Fe@PbI_2$), meanwhile the triangular doping configuration ($3Fe@PbI_2$) induces antiparallel spin coupling with the IMA. Codoping with Br atoms can enhance the thermodynamic stability and tune the system magnetism. Specifically, Br codoping induces the ferromagnetic-to-antiferromagnetic state transition in the $2Fe@PbI_2$ system and enhances the antiparallel spin coupling in the $3Fe@PbI_2$ system. Moreover, the PMA and IMA in these systems, respectively, are also affected, becoming weaker. In all cases of doping and codoping, the magnetic semiconductor nature with relatively large spin-dependent energy gaps is obtained. Our findings introduce the doped and codoped PbI_2 monolayer systems as new promising 2D spintronic materials with a magnetic semiconductor nature and tunable magnetic anisotropy, which can be selectively employed for magnetic field sensing and Magnetoresistive Random Access Memories (MRAMs) fabrication.

Received 19th March 2026
Accepted 27th May 2026

DOI: 10.1039/d6ra02311h

rsc.li/rsc-advances

I. Introduction

The discovery of graphene in 2004 has revolutionized materials science in fundamental research and also technological applications.[1] Graphene is a two-dimensional (2D) allotrope of carbon, in which atoms are arranged in a planar honeycomb-like configuration and bound to each other by the unique sp^2 hybridization. Graphene has intriguing properties, including high mechanical strength with excellent elasticity, high thermal and electrical conductivity, high carrier mobility, and high specific area,[2,3] among others. Therefore, researchers have paid special attention to this 2D material to explore new physical features and promising applications. However, as a disadvantage of graphene, the semimetal nature without an intrinsic band gap hinders significantly its applications in digital electronics, which causes a low on/off ratio in field-effect transistors (FETs). This limitation has motivated two separate research lines: (1) band gap opening of graphene, which can be achieved by surface functionalization,[4,5] doping,[6,7] edge engineering,[8,9] and thickness modification;[10,11] and (2) searching for new 2D semiconducting materials that has led to the discovery of large variety of 2D semiconductors. In this regard, transition metal dichalcogenides (TMDs) with relatively large band gap have been explored as promising building blocks for electronic and optoelectronic nano devices, including FETs with high on/off switching ratio,[12,13] photodetectors,[14,15] and light emitters.[16,17] Also, 2D semiconductor black phosphorus (well known as "phosphorene") with a high carrier mobility of over 1000 $cm^2 V^{-1} s^{-1}$ has emerged as an excellent alternative.[18] Many other 2D semiconductor families have been also discovered, but not limited, such as those based on III-group monochalcogenides,[19,20] IV-group momochalcogenides and dichalcogenides,[21,22] and IV-group halides,[23,24] among others. In

---

[a] *Center for Forecasting Study, Institute of Southeast Vietnamese Studies, Thu Dau Mot University, Ho Chi Minh City, Vietnam*
[b] *Faculty of Physics, TNU-University of Education, Thai Nguyen, 250000, Vietnam*
[c] *Faculty of Electronics and Telecommunications, Electric Power University, No. 235 Hoang Quoc Viet Street, Hanoi, Vietnam*
[d] *Institute of Innovation in Pharmaceutical and HealthCare Food, Thu Dau Mot University, Ho Chi Minh City, Vietnam*
[e] *Universidad Nacional Autónoma de México, Centro de Nanociencias y Nanotecnología, Apartado Postal 14, Ensenada, Baja California, Código Postal 22800, Mexico*
[f] *Institute of Theoretical and Applied Research, Duy Tan University, Ha Noi 100000, Vietnam. E-mail: dominhhoat@duytan.edu.vn*
[g] *School of Engineering and Technology, Duy Tan University, Da Nang 550000, Vietnam*

general, the electronic properties of 2D semiconductors, such as band gap and carrier mobility, can be effectively tuned by different methods such as applying external strain and electric field,[25,26] forming heterostructures,[27,28] and thickness engineering.[29,30]

On the other hand, a new class of 2D semiconductor metal halides MX_2 (M = Mg, Ca, Zn, Cd, Ge, and Pb; X = Cl, Br, and I) has been predicted by Lu *et al.*,[31] where calculations assert semiconductor nature of PbI_2 monolayer with enhanced hole effective mass compared to its bulk counterpart. Bulk PbI_2 material crystallizes in 1T layered structure, in which atomic layers are connected by weak van der Waals interactions. This structural feature has allowed preparing 2D nanosheets by exfoliation for diverse applications, including ultrafast photonics,[32] photoluminescence,[33] and high-performance UV photodetection.[34] Using the bottom-up physical vapour deposition (PVD) method, Zhong *et al.*[35] has realized successfully the growth of large-scale PbI_2 monolayer and few layers, where characterizations demonstrate the indirect-gap semiconductor of monolayer form. It has been found that the band gap decreases with direct-to-indirect gap transition when reducing the thickness of PbI_2.[36] Experimental realization of 2D PbI_2 has motivated several theoretical investigations on exploring its intriguing electronic and optical properties.[36–38] In addition, Wang *et al.*[39] have investigated the electronic band structure and magnetic properties of PbI_2 monolayer with I vacancy and nonmetallic atom doping. It has been found magnetic moments induced by I vacancy and S/P/Si impurities, meanwhile halogen doping maintains the nonmagnetic nature.

Despite the increasing experimental and theoretical attention has paid to PbI_2 monolayer, the investigations on its magnetism engineering are still lacking. In this work, doping with Fe atoms is proposed to modify the electronic properties and induce the effective magnetization of PbI_2 monolayer. It is anticipated that Fe doping leads to the emergence of magnetic semiconductor nature in PbI_2 monolayer, which is suitable for spintronic applications. Throughout the paper, the interactions between Fe impurity and the host monolayer are presented and discussed, which are the main origin of electronic modification and magnetism. In addition, the spin coupling and magnetic anisotropy are also studied to provide deep insights into the induced magnetism.

II. Computational details

As implemented in Vienna *ab initio* simulation package (VASP),[40,41] the projector augmented wave (PAW) method with potpaw.54 pseudopotential set is employed to carry out first-principles calculations on the structural, electronic, and magnetic properties of pristine and Fe/Br-doped PbI_2 monolayer. This method works within the framework of density functional theory (DFT),[42] where electron exchange-correlation is treated using Perdew–Burke–Ernzerhof scheme of the generalized gradient approximation (GGA-PBE).[43] The $6s^26p^2$ states of Pb atom, $5s^25p^5$ states of I atom, $4s^24p^5$ states of Br atom, and $3d^64s^2$ states of Fe atom are treated as valence states. To describe properly the highly correlated Fe-3d electrons, DFT+U approach by Dudarev *et al.*[44] is adopted using the rotationally invariant effective parameter $U_{\text{eff}} = U - J = 4.0$ eV, where U and J are on-site Coulomb parameter and exchange parameter, respectively. This value has been confirmed to be suitable for all 3d transition metals.[45] Wave functions are expanded using the plane-wave basis set truncated by a kinetic energy cutoff of 500 eV. Convergence thresholds for energy and Hellmann–Feynmann force are set to 1×10^{-6} eV and 1×10^{-2} eV Å^{-1}, respectively. The Brillouin zones are sampled using Monkhost–Pack *k*-point grids[46] of $20 \times 20 \times 1$ and $4 \times 4 \times 1$ for the PbI_2 monolayer unit cell and $4 \times 4 \times 1$ supercell, respectively. A large vacuum region (more than 16 Å) is inserted in the direction perpendicular (*z*-axis) to the PbI_2 monolayer plane (*xy*-plane) to eliminate the spurious interactions between periodic neighboring layers. For the proper reproducibility, more computational details are given in Table S1 of the SI.

The formation energy E_f of the doped PbI_2 monolayer systems is calculated using following expression:

$$E_f = \frac{E(\text{d-PbI}_2) - E(\text{p-PbI}_2) + n_{\text{Pb/I}}\mu_{\text{Pb/I}} - n_{\text{Fe/Br}}\mu_{\text{Fe/Br}}}{n_{\text{Pb}} + n_{\text{I}}} \quad (1)$$

$E(\text{d-PbI}_2)$ and $E(\text{p-PbI}_2)$ are total energy of the doped and pristine PbI_2 monolayer, respectively; $n_{\text{Pb/I}}$ and $n_{\text{Fe/Br}}$ denote number of the replaced Pb/I atoms and incorporated Fe/Br atoms ($n_{\text{Pb}} = n_{\text{Fe}}$ and $n_{\text{I}} = n_{\text{Br}}$), respectively; $\mu_{\text{Pb/I}}$ and $\mu_{\text{Fe/Br}}$ denote chemical potential of Pb/I and Fe/Br atoms, respectively. Herein, chemical potential of Pb and Fe atoms is calculated from their most stable bulk phase, while that of halide atoms is determined from their respective molecules. It is assumed that the doping is realized in a rich-Fe condition, which is thermodynamically favorable. In addition, their cohesive energy E_c is also computed as follows:

$$E_c = \frac{E(\text{d-PbI}_2) - \sum_{\text{Pb,I,Fe,Br}} m_{\text{Pb,I,Fe,Br}} E(\text{Pb, I, Fe, Br})}{\sum_{\text{Pb,I,Fe,Br}} m_{\text{Pb,I,Fe,Br}}} \quad (2)$$

herein, m_i and $E(i)$ denote number of atom i in the doped system and energy of an isolated atom i (i = Pb, I, Fe, and Br), respectively.

Phonon dispersion curves are calculated using finite displacement method. Corresponding calculations are performed with PHONOPY code.[47] In addition, *ab initio* molecular dynamic (AIMD) simulations are carried out in the NVT ensemble combined with Nose–Hoover thermostat.[48,49] Herein, 2500 simulations steps are recorded with time step of 2 fs for lasting total time of 5 ps.

III. Results and discussion

A. Stability and electronic properties of PbI_2 monolayer

Fig. 1a shows trigonal unit cell of PbI_2 monolayer in 1T phase, which can be represented with $P\bar{3}m1$ space group. It can be seen that an atomic sheet of Pb atom is sandwiched between two atomic sublayers of I atoms to form I–Pb–I atomic sequence. Each Pb atom occupies an octahedral site formed by six I atoms. After the structural relaxation, PbI_2 monolayer unit cell is described by following parameters: (1) lattice constant $a = 4.67$

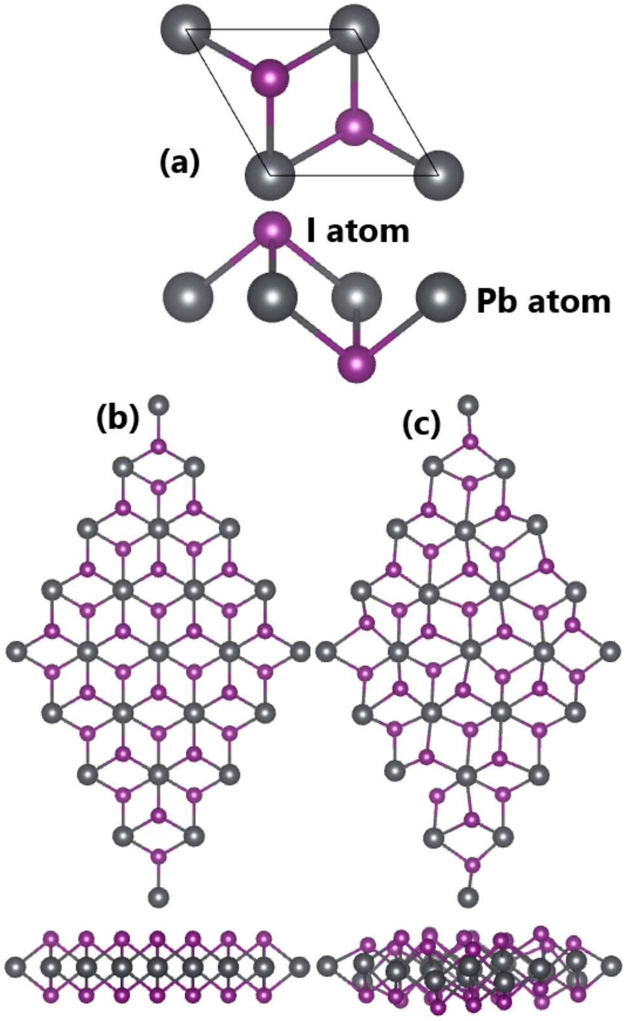

Fig. 1 Atomic structure of PbI_2 monolayer in (a) a unit cell, (b) 4 × 4 × 1 supercell at equilibrium, and (c) 4 × 4 × 1 supercell after AIMD simulations.

Å; (2) chemical bond length $d_{\text{Pb–I}} = 3.27$ Å; (3) monolayer thickness $\Delta = 2 \times \Delta_{\text{Pb–I}} = 2 \times 1.85 = 3.70$ Å; and (4) interatomic angles $\angle\text{PbIPb} = 91.07°$ and $\angle\text{IPbI} = 88.93°$. Some of them, including lattice constant and chemical bond length, are in good agreement with previous studies,[36,37] confirming their reliability. In the following, the stability of PbI_2 monolayer is studied:

- The dynamical stability of PbI_2 monolayer is assessed by its phonon dispersion spectrum. The calculated results are displayed in Fig. 2a. From the figure, only tiny imaginary phonon modes are observed, which can be attributed to the numerical error. Importantly, the absence of significant imaginary frequencies confirms that PbI_2 monolayer is dynamically stable.

- The thermal stability of PbI_2 monolayer is examined by means of *ab initio* molecular dynamics (AIMD) simulations, using a 4 × 4 × 1 supercell. Fig. 2b depicts the evolution of temperature and system energy during 5 ps of AIMD simulations. Note that these parameters exhibit small fluctuation without abrupt variation. In addition, the atomic structure and chemical bonds are well maintained as visualized in Fig. 1c. These findings demonstrate that PbI_2 monolayer is thermally stable.

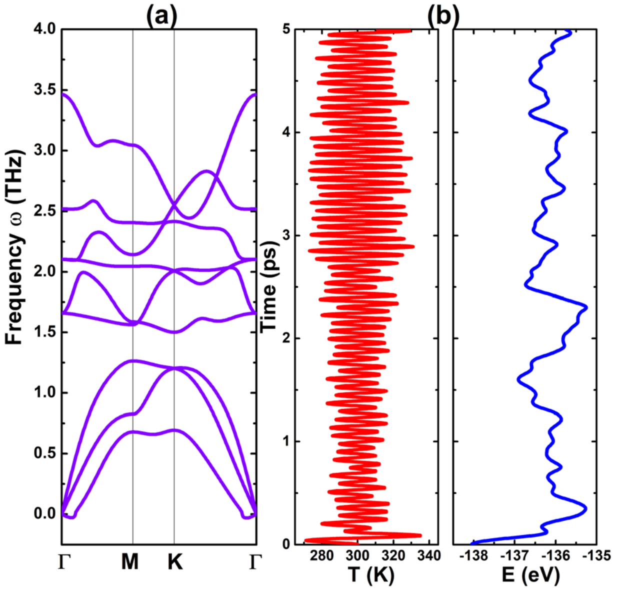

Fig. 2 (a) Phonon dispersion curves and (b) fluctuation of temperature and energy during AIMD simulations of PbI_2 monolayer.

- The mechanical stability of PbI_2 monolayer is evaluated through elastic constants C_{11} and C_{12} that should satisfy Born criteria:[50] $C_{11} > 0$ and $C_{11} > |C_{12}|$. Herein, elastic constants are derived from the second-order derivatives of the system energy with respect to strain, where their relationship is determined by calculating energy at several small strains applied to the lattice. Our calculations provide values of 14.688 and 3.535 N m^{-1} for C_{11} and C_{12}, respectively. These results indicate that PbI_2 monolayer is mechanically stable.

After confirmed good stability of PbI_2 monolayer, its orbital-resolved band structure is computed. From Fig. 3a, it can be seen the highest point of valence band along Γ–K path, while the lowest point of conduction band takes place at Γ point. This band structure profile indicates the indirect-gap semiconductor nature of PbI_2 monolayer, whose energy gap is calculated to be 2.50 eV that is in good agreement with previous studies.[31] Since Pb is a heavy atom, we also calculate the monolayer band gap with spin–orbit coupling (SOC). From PBE + SOC calculations, a value of 1.89 eV is obtained, which is smaller than PBE-based result due to the strong relativistic effects. The band gap is determined by the hybridized Pb-s + I-$p_{x,y,z}$ states at upper part of the valence band and Pb-p_z state at lower part of the conduction band. Moreover, in the considered energy range, the band structure is also formed by I-$p_{x,y,z}$ (at low-energy region of valence band) and Pb-$p_{x,y,z}$ (at high-energy region of conduction band) states. It is important mentioning that Pb–I bonding has covalent character generated by the electronic hybridization between Pb-6s and I-5p orbitals, and also ionic character generated by the different electronegativities of Pb and I atoms. The ionic character of Pb–I chemical bond is confirmed by

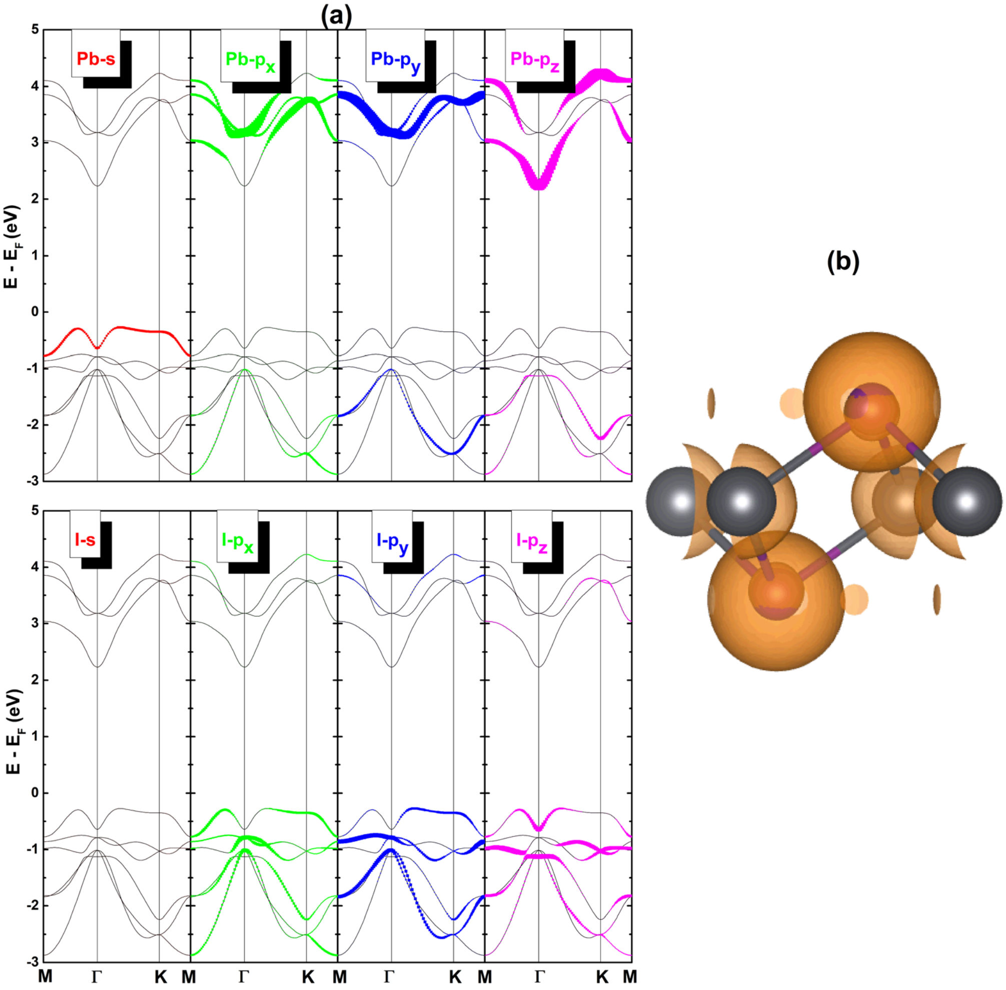

Fig. 3 (a) Orbital-resolved band structure (E_F: Fermi level) and (b) electron localization function (iso-surface value: 0.8 e Å^{-3}) of PbI_2 monolayer.

electron localization function illustrated in Fig. 3b, from which it can be seen that the concentration of charge at I atom because of its more electronegative nature compared to Pb atom. In addition, Bader charge analysis asserts that each Pb atom transfers charge amount of 0.90 e to I atoms, that is each I atom attracts 0.45 e.

B. Effects of single Fe impurity

In this part, the effects of single Fe impurity on the PbI_2 monolayer electronic and magnetic properties are investigated. The doped system is denoted by 1Fe@PbI_2, whose formation energy is calculated to be 0.51 eV per atom that represents the necessary energy to replace one Pb atom in the lattice of PbI_2 monolayer by one Fe atom. Moreover, a negative cohesive energy of −2.85 eV per atom of 1Fe@PbI_2 system suggests its good structural-chemical stability. Bader charge is calculated for Fe impurity to study its electronic interactions with the host monolayer. It is found that Fe atom loses a charge quantity of 0.93 e, which is a consequence of its metallic nature, that is Fe atom is less electronegative than its nearest neighboring I atoms. This charge transfer process from Fe impurity to the host PbI_2 monolayer is further confirmed by means of the

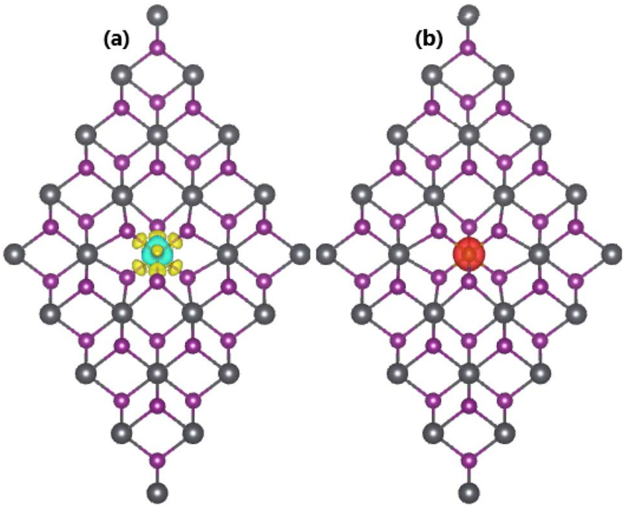

Fig. 4 (a) Charge density difference (iso-surface value: 0.005 e Å^{-3}; yellow iso-surface: charge enrichment; aqua iso-surface: charge depletion) and (b) spin density (iso-surface value: 0.01 e Å^{-3}) of 1Fe-doped PbI_2 monolayer.

charge density difference $\Delta\rho$ defined by: $\Delta\rho = \rho(1\text{Fe@PbI}_2) - \rho(\text{PbI}_2) - \rho(1\text{Fe})$, where $\rho(1\text{Fe@PbI}_2)$, $\rho(\text{PbI}_2)$, and $\rho(1\text{Fe})$ refer to the charge density of the doped system, PbI_2 monolayer, and single Fe atom, respectively. Fig. 4a visualizes the charge density difference in 1Fe@PbI_2 system. Note that the charge is depleted from Fe impurity and enriched around I atoms closest to the doping site.

As expected, Fe doping induces significant magnetism in PbI_2 monolayer with an obtained total magnetic moment of 4.00 μ_B, where large local value of 3.61 μ_B suggests that Fe atom produces primarily the system magnetic moment. Fig. 4b illustrates the spin density ρ_s in 1Fe@PbI_2 system, which is defined as difference of spin-up and spin-down charge density as follows: $\rho_s = \rho^{\uparrow} - \rho^{\downarrow}$. Note that spin iso-surfaces are centered mostly at doing site, confirming again key role on Fe atom in magnetizing PbI_2 monolayer. In order to determine the magnetic anisotropy of 1Fe@PbI_2 system, which is an essential property to determine the thermal stability and storage density, magnetic anisotropy energy (MAE) is calculated using following expression:

$$\text{MAE} = E[100] - E[001] \tag{3}$$

herein, $E[100]$ and $E[001]$ are system energies calculated through following two-step approach: (1) self-consistent calculations without spin–orbit coupling (SOC) to obtain the charge density; (2) non-self-consistent calculations with SOC, where the easy magnetization axis is set along [100] (in-plane) and [001] (out-of-plane) directions, respectively. According to our calculations, 1Fe@PbI_2 system has a negative MAE value of -353.23 μeV that indicates its in-plane magnetic anisotropy (IMA) – a feature suitable for magnetic field sensing applications. It is important mentioning that MAE values of -353.23 and -353.24 μeV are obtained when setting the energy criterion to 1×10^{-7} and 1×10^{-8} eV, respectively. These results suggest the reliability of the employed 1×10^{-6} eV criterion. Moreover, MAE value is found to become slightly less negative according to decrease the doping level as modeled by different supercell sizes (see Table S2 of the SI).

The spin-resolved band structure and projected density of states (PDOS of Fe impurity and its first neighboring I atom and second neighboring Pb atom) are given in Fig. 5. It can be seen notable spin polarization at the upper part of valence band and the lower part of conduction band, indicating the unbalanced charge distribution between spin channels to produce magnetism. Importantly, 1Fe@PbI_2 system exhibits semiconductor character in both spin configurations with spin-up and spin-down energy gaps of 2.37 and 2.42 eV, respectively. These findings confirm the magnetic semiconductor nature of the doped system. The spin asymmetry at the upper part of valence band can be attributed to Fe-d_{xy}–d_{xz}–$d_{x^2-y^2}$ states (in spin-up channel) and Fe-d_{z^2} state (in spin-down channel), where small contribution of Pb-s and I-$P_{x,y,z}$ states is also observed in both spin channels. In the low-energy region of conduction band, Fe atom shows strong spin polarization with the appearance of Fe-d_{xy}–$d_{x^2-y^2}$ states in spin-down channel. Results demonstrate that electronic properties of 1Fe@PbI_2 system are regulated mainly by the interactions of Fe impurity and its neighboring atoms. It is worth mentioning that 4 × 4 × 1 supercell is large enough to avoid the interactions between Fe impurity and its periodic image, which is confirmed by the calculations of spin-resolved band structure using different supercell sizes. Results are given in Fig. S1 of the SI. Note that the band structure profile is quite similar for 3 × 3 × 1, 4 × 4 × 1, and 5 × 5 × 1 supercell.

Practically, the charge state of defects may influence significantly on the physical properties and functionality of the doped systems.[51–53] Therefore, the spin-resolved band structure of 1Fe@PbI_2 system is also calculated at -1 and +1 charge state of impurity. It is found that the Fermi level increases drastically with -1 state, while only small decrease of this parameter is

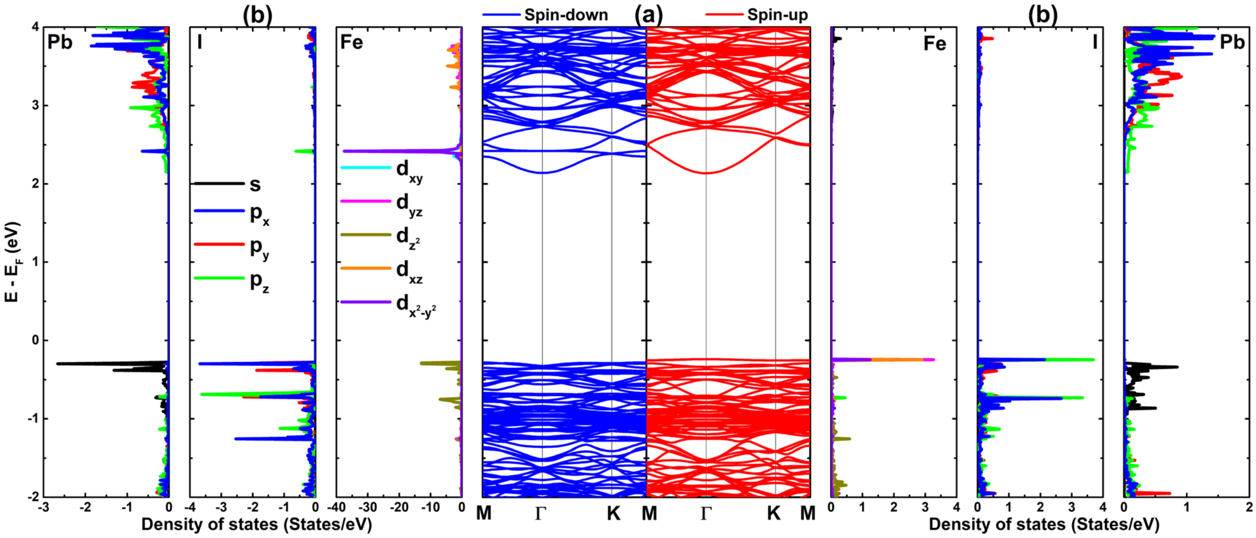

Fig. 5 (a) Spin-resolved band structure and (b) projected density of states (Fe impurity and its nearest neighboring I and Pb atoms; right side: spin-up; left side: spin-down) of 1Fe-doped PbI_2 monolayer (E_F: Fermi level).

noted in the case of +1 state (see Fig. S2 of the SI). From the calculated spin-resolved band structures given in Fig. S3, it can be noted the appearance of new energy states around the Fermi level in both cases of charged impurity to tune considerably the spin-dependent energy gaps. Specifically, spin-up/spin-down values of 2.41/0.83 and 1.18/0.06 eV are obtained with +1 and −1 states of Fe impurity, respectively.

C. Spin coupling and effects of codoping with Br atom

Now, the spin coupling between Fe impurities is studied by considering two Fe atoms in PbI_2 monolayer supercell. In this regard, the doped system is denoted by $2Fe@PbI_2$. In addition, codoping with Br atom (more electronegative than I atom but with similar valence electronic configurations) is proposed to tune the magnetic properties. Herein, we employ the notation $2Fe+Br@PbI_2$ to refer to the codoped system. Firstly, stable spin coupling is determined by calculating the system energy with Fe impurities exhibiting parallel spin configuration (ferromagnetic FM state) and antiparallel spin alignment (antiferromagnetic AFM state). Our calculations demonstrate the stability of ferromagnetic state in $2Fe@PbI_2$ system, exhibiting an energy of 17.57 meV smaller than that of antiferromagnetic state as displayed in Fig. 6a. In this case, Curie temperature T_C is estimated using the mean-field approximation as follows:

$$T_C = \frac{-2\Delta E}{3Nk_B} \tag{4}$$

where $\Delta E = 17.57$ meV; k_B is Boltzmann constant; and $N = 2$ is number of Fe atoms in the supercell. From this equation, a T_C value of 70 K is obtained. The presence of Br impurity induces the FM-to-AFM state transition, such that AFM state becomes stable in $2Fe+Br@PbI_2$ system with an energy difference of 16.01 meV in comparison with that of FM state (see Fig. 6b).

Previously, triangular doping configuration of transition metal impurities has been realized successfully in TMD monolayers.[54] Therefore, we propose a Fe triangular substitution in PbI_2 monlayer, which is denoted by $3Fe+@PbI_2$. From Fig. 7a, it can be seen that the antiparallel coupling (formed by two Fe atoms with positive spin value and the remaining one with negative spin value) has smaller energy than the parallel configuration (formed by all three Fe atoms with positive spin value). In this case, the energy difference is calculated to be 16.51 meV. The antiparallel coupling becomes stronger after incorporating Br atom since the energy difference increases to 28.57 meV (of $3Fe+Br@PbI_2$ system) as illustrated in Fig. 7b. From these results, it can be concluded that Br atom favors the antiparallel spin coupling between Fe atoms in both cases of two and three Fe impurities.

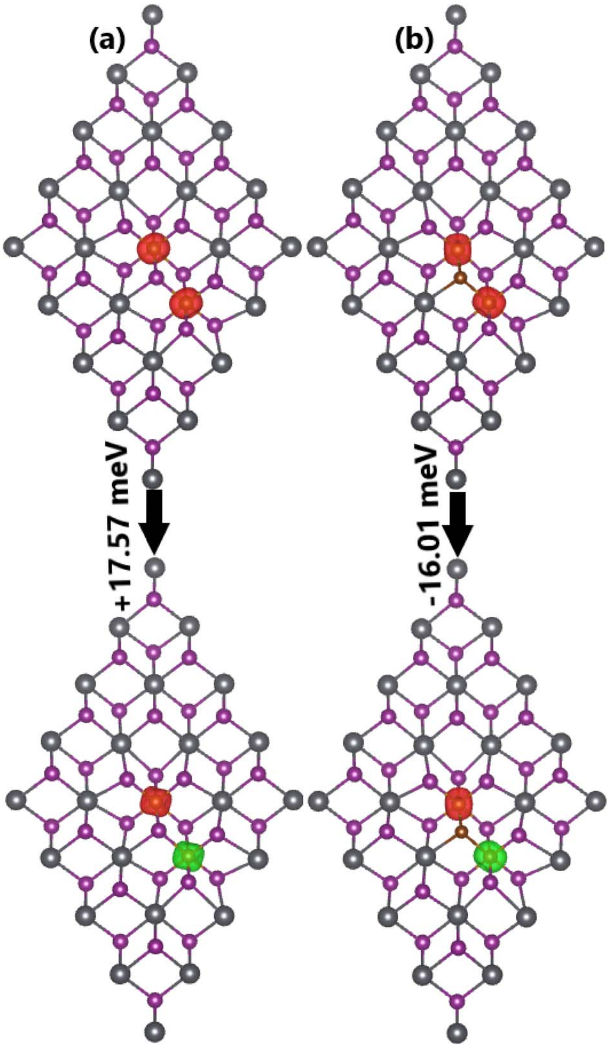

Fig. 6 Spin density (iso-surface value: 0.01 e Å^{-3}; red iso-surface: positive spin density; green iso-surface: negative spin density) and energy of magnetic phase transition of (a) 2Fe- and (b) 2Fe+Br-doped PbI_2 monolayer.

The magnetic anisotropy energy of $2Fe@PbI_2$ and $2Fe+Br@PbI_2$ systems is calculated to be 278.56 and 204.58 μeV, respectively, indicating their perpendicular magnetic anisotropy (PMA). Note that the PMA becomes weaker with Br atom considering the MAE reduction. In contrast, the IMA is found in $3Fe@PbI_2$ and $3Fe+Br@PbI_2$ systems confirmed by negative MAE values of −686.34 and −197.89 μeV, respectively. These results also confirm that the IMA is stronger in former system since Br codoping makes much less negative MAE value. These findings suggest promise of $2Fe@PbI_2$ and $2Fe+Br@PbI_2$ systems for MRAMs fabrication, while $3Fe@PbI_2$ and $3Fe+Br@PbI_2$ systems can be used in magnetic field sensing applications.

From the E_f results listed in Table 1, it can be seen that the doping process becomes thermodynamically less favorable when increasing the Fe doping level. Specifically, formation energy of $2Fe@PbI_2$ and $3Fe@PbI_2$ systems are 0.60 and 1.09 eV per atom, respectively. However, the additional incorporation of Br atom is found to favor the Fe doping by reducing considerably the formation energy to 0.39 ($2Fe+Br@PbI_2$ system) and 0.50 eV per atom ($3Fe+Br@PbI_2$ system), respectively. In addition, all four doped and codoped systems are confirmed to have good structural-chemical stability with negative E_c values between −2.88 and −2.84 eV per atom.

The spin-resolved band structures of $2Fe@PbI_2$ and $2Fe+Br@PbI_2$ systems are given in Fig. 8. The FM state of

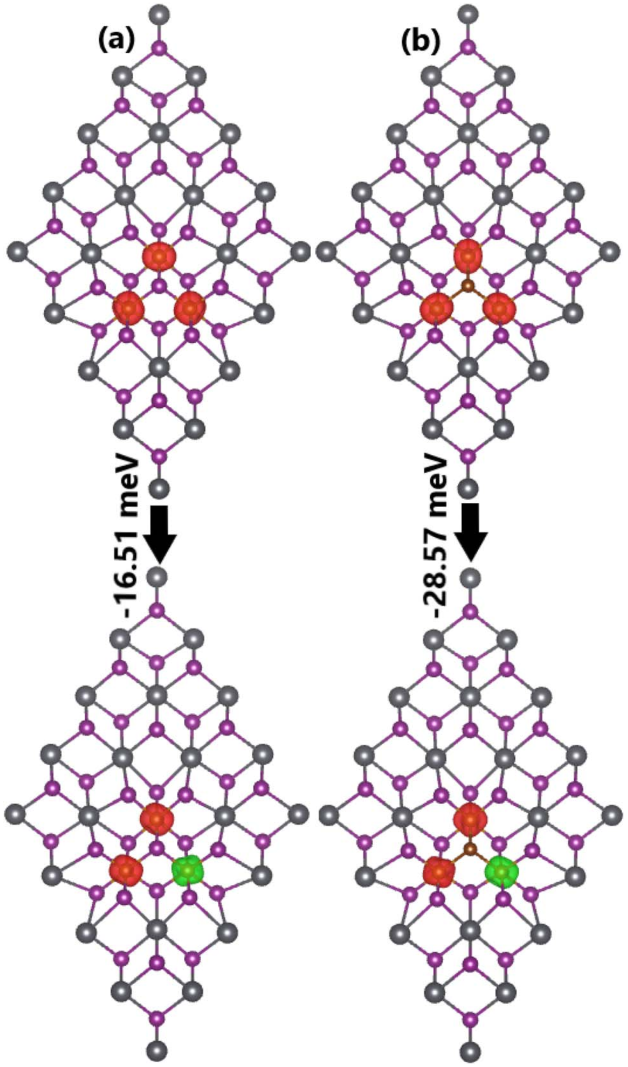

Fig. 7 Spin density (iso-surface value: 0.01 *e* Å^{-3}; red iso-surface: positive spin density; green iso-surface: negative spin density) and energy of magnetic phase transition of (a) 3Fe- and (b) 3Fe+Br-doped PbI_2 monolayer.

Table 1 Energy of magnetic phase transition $\Delta E = E_{antiparallel} - E_{parallel}$ (meV), total magnetic moment M_t (μ_B), magnetic anisotropy energy MAE $= E_x - E_z$ (μeV), formation energy E_f (eV per atom), cohesive energy E_c (eV per atom), and spin-dependent energy gap (spin-up/spin-down, eV) of the doped PbI_2 monolayer systems with different doping types

	ΔE	M_t	MAE	E_f	E_c	E_g
1Fe-		4.00	−353.23	0.51	−2.85	2.37/1.42
2Fe-	17.57	8.00	278.56	0.60	−2.85	2.11/2.33
2Fe+Br-	−16.01	0.00	204.58	0.39	−2.85	2.07/2.07
3Fe-	−16.51	4.00	−686.34	1.09	−2.88	1.81/1.90
3Fe+Br-	−28.57	4.00	−197.89	0.50	−2.84	2.10/1.98

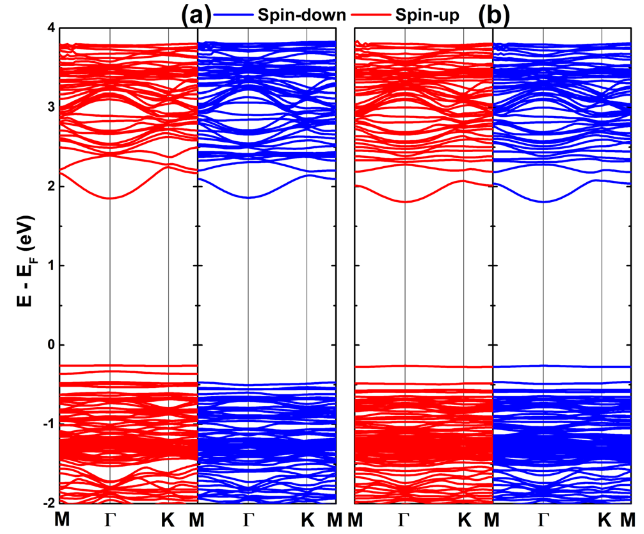

Fig. 8 Spin-resolved band structure of (a) 2Fe- and (b) 2Fe+Br-doped PbI_2 monolayer (E_F: Fermi level).

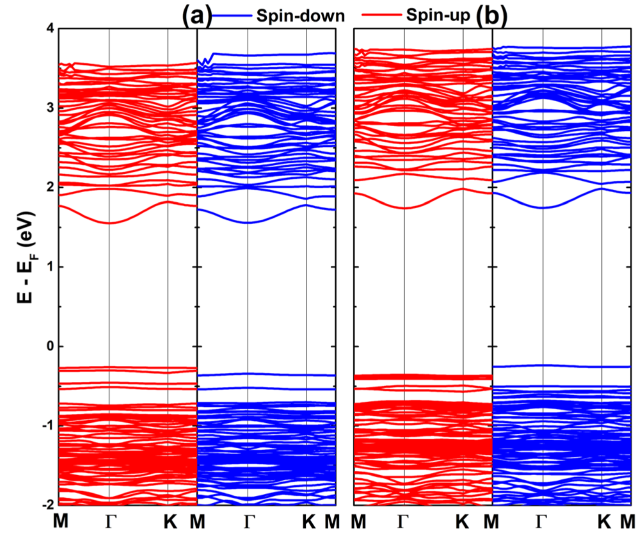

Fig. 9 Spin-resolved band structure of (a) 3Fe- and (b) 3Fe+Br-doped PbI_2 monolayer (E_F: Fermi level).

2Fe@PbI_2 system with total magnetic moment of 8.00 μ_B is reflected its strong spin polarization, mostly at the upper part of valence band. In contrast, the band structure of 2Fe+Br@PbI_2 system is spin-symmetric, corresponding to its AFM state with zero overall magnetic moment. Otherwise, the spin-asymmetric profile is observed in the band structures of 3Fe@PbI_2 and 3Fe+Br@PbI_2 systems as results of their non-zero magnetic moment (4.00 μ_B). It is important to note that the magnetic semiconductor nature is obtained by all four doping configurations (see also Fig. 9), endowing PbI_2 monolayer promise for spintronic applications. The spin-dependent energy gaps of the doped and codoped PbI_2 monolayer systems are given in Table 1.

IV. Conclusions

In summary, first-principles calculations have been performed to investigate the electronic and magnetic properties of pristine, Fe-doped, and Fe+Br-codoped PbI_2 monolayer. Through phonon calculations, AIMD simulations, and elastic constants, good structural stability of PbI_2 is confirmed. This is a 2D semiconductor, whose Pb–I chemical bond exhibits both covalent and ionic character. Covalent character is generated by the electronic hybridization between Pb-6s and I-5p orbitals, while the charge transfer from Pb atom to I atoms originates the ionic character. Effective magnetism engineering is achieved by Fe doping, where Fe-3d electrons produce mainly the system magnetism and originate the mid-gap flat subbands to regulate the magnetic semiconductor. Once incorporated into PbI_2 monolayer lattice, Fe atom transfers charge to the host monolayer as a consequence of its much more electronegative environment. Single Fe atom doping and triangular doping lead to the emergence of the IMA that is suitable for magnetic field sensing. Meanwhile, the PMA – desirable for MRAMs fabrication – is obtained by considering two-impurities doping configuration. The spin coupling is also found to differ depending on the doping level, where Br codoping favors the antiparallel spin alignment in both cases of two- and three-Fe-impurities cases. Interestingly, the presence of Br impurity can enhance the thermodynamic stability, making more feasible the realization of Fe doping in experiments. Calculations also confirm good structural-chemical stability of the doped/codoped PbI_2 monolayer systems. Our results demonstrate the effectiveness of Fe doping method for the PbI_2 monolayer magnetism engineering towards selective spintronic applications. Moreover, Br codoping can be also suggested to make antiferromagnetic semiconductor from Fe-doped systems.

Conflicts of interest

The authors declare that they have no known competing financial interests or personal relationships that could have appeared to influence the work reported in this paper.

Data availability

Data will be provided under requesting to authors.

Supplementary information (SI): more computational details. See DOI: https://doi.org/10.1039/d6ra02311h.

Acknowledgements

Calculations were performed in DGCTIC-UNAM Supercomputing Center (project LANCAD-UNAM-DGTIC-368).

References

1 K. S. Novoselov, A. K. Geim, S. V. Morozov, D.-e. Jiang, Y. Zhang, S. V. Dubonos, I. V. Grigorieva and A. A. Firsov, *Science*, 2004, **306**(5696), 666–669.
2 D. Abergel, V. Apalkov, J. Berashevich, K. Ziegler and T. Chakraborty, *Adv. Phys.*, 2010, **59**(4), 261–482.
3 A. D. Ghuge, A. R. Shirode and V. J. Kadam, *Curr. Drug Targets*, 2017, **18**(6), 724–733.
4 M. Pumera and C. H. A. Wong, *Chem. Soc. Rev.*, 2013, **42**(14), 5987–5995.
5 H. Zhang, E. Bekyarova, J.-W. Huang, Z. Zhao, W. Bao, F. Wang, R. C. Haddon and C. N. Lau, *Nano Lett.*, 2011, **11**(10), 4047–4051.
6 X. Fan, Z. Shen, A. Liu and J.-L. Kuo, *Nanoscale*, 2012, **4**(6), 2157–2165.
7 P. Rani and V. Jindal, *RSC Adv.*, 2013, **3**(3), 802–812.
8 M. Y. Han, B. Özyilmaz, Y. Zhang and P. Kim, *Phys. Rev. Lett.*, 2007, **98**(20), 206805.
9 Y.-W. Son, M. L. Cohen and S. G. Louie, *Phys. Rev. Lett.*, 2006, **97**(21), 216803.
10 Y. Zhang, T.-T. Tang, C. Girit, Z. Hao, M. C. Martin, A. Zettl, M. F. Crommie, Y. R. Shen and F. Wang, *Nature*, 2009, **459**(7248), 820–823.
11 E. McCann and M. Koshino, *Rep. Prog. Phys.*, 2013, **76**(5), 056503.
12 D. Jiang, Z. Liu, Z. Xiao, Z. Qian, Y. Sun, Z. Zeng and R. Wang, *J. Mater. Chem. A*, 2022, **10**(1), 89–121.
13 C. Gong, H. Zhang, W. Wang, L. Colombo, R. M. Wallace and K. Cho, *Appl. Phys. Lett.*, 2013, **103**(5), 053513.
14 S. Aftab and H. H. Hegazy, *Small*, 2023, **19**(18), 2205778.
15 X. Li, S. Aftab, S. Hussain, F. Kabir, A. G. Al-Sehemi, M. Aslam, J. H. Kim and B. S. Goud, *J. Mater. Chem. C*, 2024, **12**(4), 1211–1232.
16 W. Zheng, Y. Jiang, X. Hu, H. Li, Z. Zeng, X. Wang and A. Pan, *Adv. Opt. Mater.*, 2018, **6**(21), 1800420.
17 J. Gu, B. Chakraborty, M. Khatoniar and V. M. Menon, *Nat. Nanotechnol.*, 2019, **14**(11), 1024–1028.
18 L. Li, Y. Yu, G. J. Ye, Q. Ge, X. Ou, H. Wu, D. Feng, X. H. Chen and Y. Zhang, *Nat. Nanotechnol.*, 2014, **9**(5), 372–377.
19 Z. Yang and J. Hao, *Adv. Mater. Technol.*, 2019, **4**(8), 1900108.
20 H. Cai, Y. Gu, Y.-C. Lin, Y. Yu, D. B. Geohegan and K. Xiao, *Appl. Phys. Rev.*, 2019, **6**(4), 041312.
21 Z. Hu, Y. Ding, X. Hu, W. Zhou, X. Yu and S. Zhang, *Nanotechnology*, 2019, **30**(25), 252001.
22 J. Luo, X. Song, Y. Lu, Y. Hu, X. Lv, L. Li, X. Li, J. Deng, Y. Yan, Y. Jiang, *et al.*, *J. Phys. Condens. Matter*, 2022, **34**(28), 285701.
23 C.-S. Liu, X.-L. Yang, J. Liu and X.-J. Ye, *J. Phys. Chem. C*, 2018, **122**(38), 22137–22142.
24 P. M. Tan, N. T. Son, D. K. Nguyen, J. Guerrero-Sanchez and D. Hoat, *RSC Adv.*, 2026, **16**(14), 12628–12638.
25 D. Hoat, T. V. Vu, M. M. Obeid and H. R. Jappor, *Chem. Phys.*, 2019, **527**, 110499.
26 H. Chen, C. Tan, K. Zhang, W. Zhao, X. Tian and Y. Huang, *Appl. Surf. Sci.*, 2019, **481**, 1064–1071.
27 C. Zhang, C. Gong, Y. Nie, K.-A. Min, C. Liang, Y. J. Oh, H. Zhang, W. Wang, S. Hong, L. Colombo, *et al.*, *2D Mater.*, 2017, **4**(1), 015026.
28 B. Amin, N. Singh and U. Schwingenschlögl, *Phys. Rev. B: Condens. Matter Mater. Phys.*, 2015, **92**(7), 075439.
29 J. Kang, L. Zhang and S.-H. Wei, *J. Phys. Chem. Lett.*, 2016, **7**(4), 597–602.
30 W. Jin, P.-C. Yeh, N. Zaki, D. Zhang, J. T. Sadowski, A. Al-Mahboob, A. M. van Der Zande, D. A. Chenet, J. I. Dadap, I. P. Herman, *et al.*, *Phys. Rev. Lett.*, 2013, **111**(10), 106801.

31 F. Lu, W. Wang, X. Luo, X. Xie, Y. Cheng, H. Dong, H. Liu and W.-H. Wang, *Appl. Phys. Lett.*, 2016, **108**(13), 132104.

32 Q. Fan, J. Huang, N. Dong, S. Hong, C. Yan, Y. Liu, J. Qiu, J. Wang and Z. Sun, *ACS Photonics*, 2019, **6**(4), 1051–1057.

33 C. Cong, J. Shang, L. Niu, L. Wu, Y. Chen, C. Zou, S. Feng, Z.-J. Qiu, L. Hu, P. Tian, *et al.*, *Adv. Opt. Mater.*, 2017, **5**(21), 1700609.

34 H. Xiao, T. Liang and M. Xu, *Small*, 2019, **15**(33), 1901767.

35 M. Zhong, S. Zhang, L. Huang, J. You, Z. Wei, X. Liu and J. Li, *Nanoscale*, 2017, **9**(11), 3736–3741.

36 D. Hoat, T. V. Vu, M. M. Obeid and H. R. Jappor, *Superlattice. Microst.*, 2019, **130**, 354–360.

37 M. Naseri, D. Hoat, K. Salehi and S. Amirian, *J. Mol. Graph. Model.*, 2020, **95**, 107501.

38 R. Ran, C. Cheng, Z.-Y. Zeng, X.-R. Chen and Q.-F. Chen, *Philos. Mag.*, 2019, **99**(10), 1277–1296.

39 Y. Wang, C. Xu, J. Zhang, X. Du and Y. Yan, *J. Magn. Magn Mater.*, 2018, **463**, 36–43.

40 G. Kresse and J. Furthmüller, *Comput. Mater. Sci.*, 1996, **6**(1), 15–50.

41 G. Kresse and J. Furthmüller, *Phys. Rev. B: Condens. Matter Mater. Phys.*, 1996, **54**(16), 11169.

42 W. Kohn and L. J. Sham, *Phys. Rev.*, 1965, **140**(4A), A1133.

43 J. P. Perdew, K. Burke and M. Ernzerhof, *Phys. Rev. Lett.*, 1996, **77**(18), 3865.

44 S. L. Dudarev, G. A. Botton, S. Y. Savrasov, C. Humphreys and A. P. Sutton, *Phys. Rev. B: Condens. Matter Mater. Phys.*, 1998, **57**(3), 1505.

45 S. Pakdel, T. Olsen and K. S. Thygesen, *npj Comput. Mater.*, 2025, **11**(1), 18.

46 H. J. Monkhorst and J. D. Pack, *Phys. Rev. B*, 1976, **13**(12), 5188.

47 A. Togo, L. Chaput, T. Tadano and I. Tanaka, *J. Phys. Condens. Matter*, 2023, **35**(35), 353001.

48 S. Nosé, *J. Chem. Phys.*, 1984, **81**(1), 511–519.

49 W. G. Hoover, *Phys. Rev. A: At., Mol., Opt. Phys.*, 1985, **31**(3), 1695.

50 F. Mouhat and F.-X. Coudert, *Phys. Rev. B: Condens. Matter Mater. Phys.*, 2014, **90**(22), 224104.

51 C. Yang, C. Yang, H. Yan, G. Ge, W. Wang and P. Ou, *J. Mater. Chem. A*, 2025, **13**(45), 39032–39041.

52 W. Wentao, Y. Qu, D. Li, A. Zhang, H. Yan, Z. Feng and W. Yao, *Int. J. Hydrogen Energy*, 2024, **79**, 702–714.

53 J. Zhang, Y. Liu, C. Yang, Y. Qu, A. Zhang, Z. Feng, W. Wang and P. Ou, *J. Catal.*, 2025, **447**, 116135.

54 D. Shen, B. Zhao, Z. Zhang, H. Zhang, X. Yang, Z. Huang, B. Li, R. Song, Y. Jin, R. Wu, *et al.*, *ACS Nano*, 2022, **16**(7), 10623–10631.